



Theoretical calculations of hyperfine splitting, Zeeman shifts, and isotope shifts of $^{27}\text{Al}^+$ and logical ions in Al^+ clocks

Xiao-Kang Tang(唐晓康), Xiang Zhang(张祥), Yong Shen(沈咏), and Hong-Xin Zou(邹宏新)

Citation: Chin. Phys. B, 2021, 30 (12): 123204. DOI: 10.1088/1674-1056/ac0130

Journal homepage: <http://cpb.iphy.ac.cn>; <http://iopscience.iop.org/cpb>

What follows is a list of articles you may be interested in

Anisotropic exciton Stark shift in hemispherical quantum dots

Shu-Dong Wu(吴曙东)

Chin. Phys. B, 2021, 30 (5): 053201. DOI: 10.1088/1674-1056/abd472

Precision measurements with cold atoms and trapped ions

Qiuxin Zhang(张球新), Yirong Wang(王艺蓉), Chenhao Zhu(朱晨昊), Yuxin Wang(王玉欣), Xiang Zhang(张翔), Kuiyi Gao(高奎意), Wei Zhang(张威)

Chin. Phys. B, 2020, 29 (9): 093203. DOI: 10.1088/1674-1056/aba9c6

Photoelectron imaging on vibrational excitation and Rydberg intermediate states in multi-photon ionization process of NH_3 molecule

Ya-Nan Sun(孙亚楠), Yan-Hui Wang(王艳辉), Le-Le Song(宋乐乐), Hai-Bin Du(杜海滨), Xiao-Chun Wang(王晓春), Lan-Lai He(赫兰海), Si-Zuo Luo(罗嗣佐), Qin Yang(杨钦), Jing Leng(冷静), Fu-Chun Liu(刘福春)

Chin. Phys. B, 2020, 29 (9): 093201. DOI: 10.1088/1674-1056/ab9431

Theoretical investigation on forbidden transition properties of fine-structure splitting in ^2D state for K-like ions with $26 \leq Z \leq 36$

Jian-Peng Liu(刘建鹏), Cheng-Bin Li(李承斌), Hong-Xin Zou(邹宏新)

Chin. Phys. B, 2017, 26 (10): 103201. DOI: 10.1088/1674-1056/26/10/103201

Spectrally selective optical pumping in Doppler-broadened cesium atoms

Zhang Jun-Hai, Zeng Xian-Jin, Li Qing-Meng, Huang Qiang, Sun Wei-Min

Chin. Phys. B, 2013, 22 (5): 053202. DOI: 10.1088/1674-1056/22/5/053202

Theoretical calculations of hyperfine splitting, Zeeman shifts, and isotope shifts of $^{27}\text{Al}^+$ and logical ions in Al^+ clocks*

Xiao-Kang Tang(唐晓康), Xiang Zhang(张祥), Yong Shen(沈咏), and Hong-Xin Zou(邹宏新)[†]

College of Liberal Arts and Sciences, National University of Defense Technology, Changsha 410073, China

(Received 23 February 2021; revised manuscript received 10 May 2021; accepted manuscript online 14 May 2021)

Based on the multiconfiguration Dirac–Hartree–Fock (MCDHF) method, similar models are employed to simultaneously calculate the first-order and second-order Zeeman coefficients as well as the hyperfine interaction constants of the related energy levels of $^{27}\text{Al}^+$ and its logical ions $^9\text{Be}^+$ and $^{25}\text{Mg}^+$ in the $^{27}\text{Al}^+$ optical clock. With less than 0.34% deviations from experimental values in Zeeman coefficients of $^{27}\text{Al}^+$, these calculated parameters will be of great help for better evaluation of the systematic uncertainty. We also calculate the isotope shift parameters of the related energy levels, which could extend our knowledge and understanding of nuclear properties of these ions.

Keywords: Zeeman effect, isotope shift, aluminum ion optical clock, MCDHF method

PACS: 32.60.+i, 31.30.Gs, 32.10.Fn, 31.15.ac

DOI: 10.1088/1674-1056/ac0130

1. Introduction

Nowadays, the ultra-high precision optical clock systems have played an important role in the fields of metrology, satellite navigation, deep space exploration, very long baseline interference (VLBI), basic physical law inspection, *etc.* Especially for physics research, there are many characteristic applications, for example, the measurements on the temporal variation of the fine-structure constant and the proton-to-electron mass ratio,^[1,2] the detections of relativistic effects such as time dilation,^[3,4] gravitational red-shift,^[5] and gravitational waves^[6] as well as the search of dark matter.^[7,8]

The uncertainty of the aluminum ion optical clock has now entered the order of 10^{-19} , which is the lowest among all current optical clocks.^[9] The $^{27}\text{Al}^+$ optical clock adopts the weak allowed transition $J = 0 \rightarrow J = 0$. Compared with other atoms, it is less sensitive to the external magnetic and electric field, and is an ideal candidate for next generation frequency standard.^[10] Since the wavelength of the electric dipole transition of $^{27}\text{Al}^+$ is 167 nm, deep in the vacuum ultraviolet band, it is difficult to achieve direct laser cooling and quantum state detection. Therefore, sympathetic cooling and quantum logic spectroscopy are currently widely adopted.^[11,12]

The related energy level structures of $^{27}\text{Al}^+$ and its two logic ions $^{25}\text{Mg}^+$ and $^9\text{Be}^+$ are shown in Fig. 1. The $^1S \rightarrow ^3P_0$ transition in $^{27}\text{Al}^+$ is the clock transition that needs to be interrogated. In experiments, $|^1S_0, m_F = 5/2\rangle \rightarrow |^3P_0, m_{F'} = 5/2\rangle$ and $|^1S_0, m_F = -5/2\rangle \rightarrow |^3P_0, m_{F'} = -5/2\rangle$ transitions are usually measured alternately to construct a “virtual” transition $|^1S_0, m_F = 0\rangle \rightarrow |^3P_0, m_{F'} = 0\rangle$ that is independent of the first-order Zeeman effect as the clock transition.^[13] Figure 1 also shows the transitions related to Raman sideband cooling,

Doppler cooling and quantum state detection for $^{25}\text{Mg}^+$ and $^9\text{Be}^+$.^[3,11,12] The transitions (green solid line) between the qubit states are first-order sensitive to the external magnetic field, while the transitions (green dashed line) between the hyperfine ground states with $m_F = 0$ are only second-order sensitive. They can be used jointly to determine the DC and AC quadratic Zeeman frequency shift.^[14] The external magnetic field is an important factor affecting the energy level structures of ions and must be taken into account.^[15] Also, the uncertainties of the quadratic Zeeman coefficient of the clock transition and the hyperfine constants of ground states in the logical ions are relevant to the evaluation of the $^{27}\text{Al}^+$ quantum-logic clock systematic uncertainty.^[14] As a result, it is necessary to measure and calculate the related energy level structures of these ions with high precision.

At present, the related theoretical calculations of $^{27}\text{Al}^+$,^[16,17] $^9\text{Be}^+$,^[18–22] and $^{25}\text{Mg}^+$ ^[23–29] have been reported, but most of these works focused on a certain energy level or a certain physical constant of a particular ion. Moreover, different calculation methods lead to different results, and the impacts are difficult to evaluate. To solve this problem, we performed a comprehensive calculation under a similar framework for the transitions involved in the clock ion $^{27}\text{Al}^+$ and its logical ions $^9\text{Be}^+$ and $^{25}\text{Mg}^+$, which can provide some important theoretical parameters to further suppress the uncertainty of the $^{27}\text{Al}^+$ optical clock.

In this paper, we calculate the hyperfine constants, Zeeman coefficients, and isotope shift parameters of related energy levels in these ions by employing the multiconfiguration Dirac–Hartree–Fock (MCDHF) method. The differences be-

*Project supported by the National Natural Science Foundation of China (Grant Nos. 11604385 and 91536106), the Natural Science Foundation of Hunan Province, China (Grant No. 2019JJ50743), and the Research Project of the National University of Defense Technology (Grant No. ZK17-03-11).

[†]Corresponding author. E-mail: hxzou@nudt.edu.cn

tween the calculated values and the experimental values of the Zeeman coefficients are all below 0.34%. These results will be helpful to analyze and evaluate the uncertainty of the optical clock system. Especially when accurate experimental values are not available, these results could be used as alternative ref-

erence values. The calculated isotope shifts can provide important parameters for the spectroscopic experiment to measure the nuclear charge radii, and help to understand the structures, properties and nucleon interaction law of these three elements.

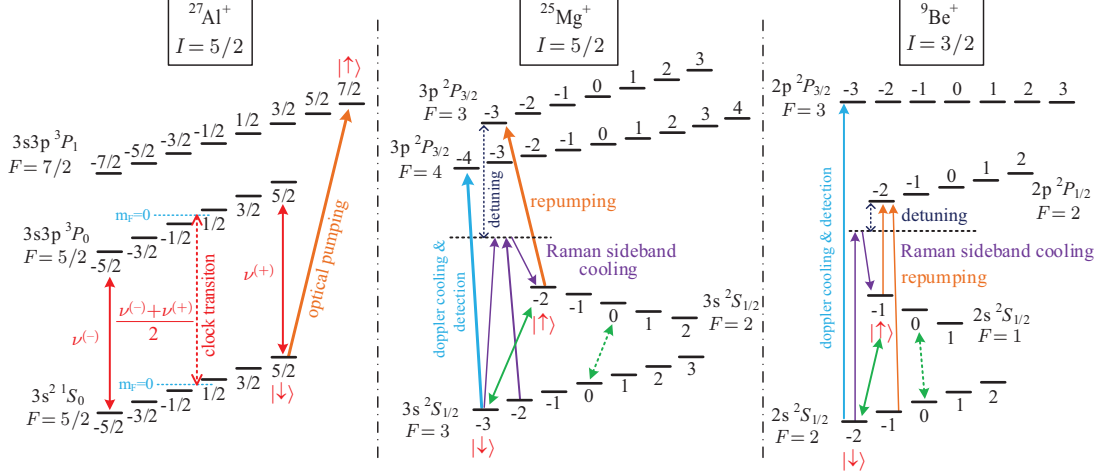


Fig. 1. Energy levels and relevant transitions of $^{27}\text{Al}^+$ and its logic ions $^9\text{Be}^+$ and $^{25}\text{Mg}^+$. The qubit states of an ion are denoted by $|\uparrow\rangle$ and $|\downarrow\rangle$.

2. Theory and computational details

2.1. Calculation theory

The process and accuracy of atomic structure calculation strictly depend on the representation of atomic states and the explicit definition of many-electron basis. In the MCDHF method, the atomic state wave functions (ASFs) are the linear combination of configuration state wave functions (CSFs) with the same parity P , total angular momentum J , and its z -axis component M_J ,^[30]

$$\Psi(\gamma P J M_J) = \sum_{i=1}^{N_{\text{CSF}}} c_i \Phi(\gamma_i P J M_J). \quad (1)$$

Here N_{CSF} is the total number of the CSFs, c_i represents the mixing coefficient, γ_i is the additional quantum number to distinguish the CSFs. The CSFs are given as coupled anti-symmetric products of one-electron orbitals

$$\phi(\mathbf{r}) = \frac{1}{r} \begin{pmatrix} P_{n\kappa}(r) \chi_{\kappa m}(\theta, \varphi) \\ i Q_{n\kappa}(r) \chi_{-\kappa m}(\theta, \varphi) \end{pmatrix}, \quad (2)$$

where n is the principal number and κ is the relativistic angular number. $P_{n\kappa}(r)$ and $Q_{n\kappa}(r)$ are the large and small component radial wave functions and $\chi_{\kappa m}(\theta, \varphi)$ is the spinor spherical harmonics. In the self-consistent field (SCF) process, using the variational method, the CSFs and the corresponding mixing coefficients are optimized by iteratively solving the equations. The calculation of ASFs is completed by GRASP2K package.^[31]

When the nuclear spin $I \neq 0$, the electrons and the electromagnetic multipole moments of the nucleus will interact to produce the hyperfine structure of an atomic energy level. The

corresponding Hamiltonian may be represented as a multipole expansion^[32]

$$H_{\text{hfs}} = \sum_{k=1} T^{(k)} \cdot M^{(k)}. \quad (3)$$

Here, $T^{(k)}$ and $M^{(k)}$ are spherical tensor operators of rank k in the spaces of electronic wavefunctions, $|\gamma J M_J\rangle$ and nuclear wavefunctions $|\nu M_1\rangle$ respectively. The $k=1$ term of the expansion represents the magnetic dipole interaction and the $k=2$ term the electric quadrupole interaction. Higher order terms are tiny and can often be neglected. The magnetic multipole tensors are

$$M^{(k)} = \mu_N \langle \nu I I | \Sigma \nabla \left(r^{(k)} C^{(k)} \right) \left(\frac{2}{k+1} g_l \mathbf{l} + g_s \mathbf{s} \right) | \nu I I \rangle, \quad (4)$$

where g_l and g_s are respectively the orbital and spin g -factors of the nucleons and $\mu_N = \mu_B/M$ is the nuclear magneton. For an N -electron atomic system, the electron tensor operators represented by the single-electron operator are

$$T^{(1)} = \sum_{j=1}^N t^{(1)}(j) = \sum_{j=1}^N -i\sqrt{2}\alpha r_j^{-2} [\alpha_j C^{(1)}(j)]^{(1)}, \quad (5)$$

$$T^{(2)} = \sum_{j=1}^N t^{(2)}(j) = \sum_{j=1}^N -r_j^{-3} C^{(2)}(j). \quad (6)$$

Here, i is the imaginary unit, α is the fine-structure constant, α is the Dirac matrix, and $C^{(k)}$ is the k -th order spherical tensor. Usually, the hyperfine splitting is considered independently for each atomic level and without the need to specify all the hyperfine level energies explicitly. Instead, with the nuclear magnetic dipole moment μ_I and electric quadrupole moment Q , the energy splitting of an atomic level into hyperfine

levels can be expressed conveniently in terms of the hyperfine interaction constants^[33,34]

$$A_J = \frac{\mu_I}{I} \frac{1}{[J(J+1)]^{1/2}} \langle \Psi(PJ) \| \mathbf{T}^{(1)} \| \Psi(PJ) \rangle, \quad (7)$$

$$B_J = 2Q \left[\frac{J(2J-1)}{(J+1)(2J+3)} \right]^{1/2} \times \langle \Psi(PJ) \| \mathbf{T}^{(2)} \| \Psi(PJ) \rangle. \quad (8)$$

And the hyperfine energy shift with regard to electronic level energy is given by

$$\Delta E_{\text{hfs}} = \frac{1}{2} A_J C + B_J \frac{\frac{3}{4} C(C+1) - I(I+1)J(J+1)}{2I(2I-1)J(2J-1)} \quad (9)$$

with $C = F(F+1) - J(J+1) - I(I+1)$ where the total angular momentum F is formed by the coupling of the nuclear I and electronic J angular momenta.

In addition to the hyperfine splitting caused by the coupling of electron spin and nucleus spin, the external magnetic field can split the energy level further. Neglecting diamagnetic contributions and the interaction of the magnetic field with the nucleus, and choosing the direction of the external magnetic field as the z direction, the magnetic (Zeeman) Hamiltonian can be written in terms of spherical tensors^[35]

$$H_{\text{mag}} = \left(\mathbf{N}^{(1)} + \Delta \mathbf{N}^{(1, \text{QED})} \right) \cdot \mathbf{B} \\ = \left(N_0^{(1)} + \Delta N_0^{(1, \text{QED})} \right) B. \quad (10)$$

Here, B is the magnetic field and the second term in the magnetic Hamiltonian above is (so-called) Schwinger's QED correction. For an N -electron atom, the electronic tensor operators are

$$\mathbf{N}^{(1)} = \sum_{j=1}^N \mathbf{n}^{(1)}(j) = \sum_{j=1}^N -i \frac{\sqrt{2}}{2\alpha} r_j \left[\alpha_j \mathbf{C}^{(1)}(j) \right]^{(1)}, \quad (11)$$

$$\Delta \mathbf{N}^{(1, \text{QED})} = \sum_{j=1}^N \Delta \mathbf{n}^{(1, \text{QED})}(j) = \sum_{j=1}^N \frac{g_s - 2}{2} \beta_j \Sigma_j, \quad (12)$$

where Σ_j is the relativistic spin-matrix, and $g_s = 2.00232$ is the g -factor of the electron spin. Wave functions for magnetic hyperfine structure substrates in an external magnetic field are expanded in a basis of the combined nuclear and atomic system^[36]

$$|\tilde{\gamma} I M_F\rangle = \sum_{\gamma J F} d_{\gamma J F} |\gamma I J F M_F\rangle, \quad (13)$$

where $|\gamma I J F M_F\rangle$ are coupled nuclear and atomic functions

$$|\gamma I J F M_F\rangle = \sum_{M_I, M_J} \langle I J M_I M_J | I J F M_F \rangle |I M_I\rangle |\gamma J M_J\rangle. \quad (14)$$

In the calculation process, the reduced hyperfine and Zeeman matrix elements are used to construct the total interaction matrix in the given basis. By diagonalizing the interaction matrix, the Zeeman energy splittings of hyperfine structure substrates

are obtained together with the expansion coefficients of the basis functions. The hyperfine interaction constants and Zeeman splittings are obtained by the HFSZEEMAN module.^[32]

The real atomic nucleus is a finite quantum system with a certain mass composed of protons and neutrons, and its charge distribution can be described by the nuclear root-mean-square charge radius. The energy shifts between spectrum lines of different isotopes are called isotope shifts (ISs), which consist of the mass shifts (MSs) due to the finite and different masses of the isotopes considered and the field shifts (FSs) caused by differences in the nuclear charge distributions of the isotopes. The isotope shift of a given transition between two isotopes, A and A' , with nuclear masses M and M' , is written as^[25,37,38]

$$\Delta E_{\text{IS}} = \left(\frac{1}{M} - \frac{1}{M'} \right) (\Delta K_{\text{NMS}} + \Delta K_{\text{SMS}}) + \Delta F \delta \langle r^2 \rangle. \quad (15)$$

Here, the first term called MS is the sum of two contributions: the normal mass shift (NMS) parameter ΔK_{NMS} and the specific mass shift (SMS) parameter ΔK_{SMS} . The second term called FS is the product of the field shift parameter ΔF and the term $\delta \langle r^2 \rangle$ the difference of the nuclear mean-square charge radii between two isotopes.^[39] The calculations of the isotope shifts are performed by the RIS module.^[40]

For the nuclei with charge number Z and mass M , the MS Hamiltonian under the $(\alpha Z)^4 m^2 / M$ approximation is

$$H_{\text{MS}} = H_{\text{NMS}} + H_{\text{SMS}}, \\ H_{\text{NMS}} = \frac{1}{2M} \sum_{j=1}^N \left(\mathbf{p}_j^2 - \frac{\alpha Z}{r_j} \alpha_j \cdot \mathbf{p}_j \right. \\ \left. - \frac{\alpha Z}{r_j} \left(\alpha_j \cdot \mathbf{C}_j^{(1)} \right) \mathbf{C}_j^{(1)} \cdot \mathbf{p}_j \right), \\ H_{\text{SMS}} = \frac{1}{2M} \sum_{j \neq k}^N \left(\mathbf{p}_j \cdot \mathbf{p}_k - \frac{\alpha Z}{r_j} \alpha_j \cdot \mathbf{p}_k \right. \\ \left. - \frac{\alpha Z}{r_j} \left(\alpha_j \cdot \mathbf{C}_j^{(1)} \right) \mathbf{C}_j^{(1)} \cdot \mathbf{p}_k \right). \quad (16)$$

Here, \mathbf{p} is the momentum operator of the electron and m is the mass of the electron. The NMS parameter K_{NMS} and the SMS parameter K_{SMS} of a given level are defined by the following expressions, respectively,

$$K_{\text{NMS}} = M \langle \Psi \| H_{\text{NMS}} \| \Psi \rangle, \\ K_{\text{SMS}} = M \langle \Psi \| H_{\text{SMS}} \| \Psi \rangle. \quad (17)$$

The field shift parameter ΔF of a given transition reads

$$\Delta F = \frac{2\pi}{3} Z \Delta |\Psi(0)|^2, \quad (18)$$

proportional to the change of the total probability density $\rho(\mathbf{0})$ at the origin

$$\Delta |\Psi(0)|^2 = \Delta \rho(\mathbf{0}) = \rho_u(\mathbf{0}) - \rho_l(\mathbf{0}) \quad (19)$$

associated with the transition between levels l and u .

2.2. Calculation models

To obtain higher calculation accuracy, it is usually necessary to capture the electron correlation sufficiently and appropriately. The active space approach is employed to systematically capture the electron correlation.^[41] The reference configurations of $^{27}\text{Al}^+$ are $3s^2\ ^1S_0$, $3s3p\ ^3P_{1,0}$, and $3s3p\ ^1P_1$. The reference configurations of $^{25}\text{Mg}^+$ are $3s\ ^2S_{1/2}$ and $3p\ ^2P_{1/2,3/2}$. The reference configurations of $^9\text{Be}^+$ is $1s^22s\ ^2S_{1/2}$ and $1s^22p\ ^2P_{1/2,3/2}$. The calculations were carried out by parity, meaning that the even and odd states of a single ion were optimized in separate SCF processes. During the calculation, the occupied orbitals $1s$, $2s$, and $2p$ of $^{27}\text{Al}^+$ and $^{25}\text{Mg}^+$ and $1s$ of $^9\text{Be}^+$ are treated as core orbitals, and the others as valence orbitals. The electron correlation can be divided into first-order and high-order correlations, the former is captured by the CSFs generated through the single (S) and double (D) substitutions from the occupied orbitals in the single reference configuration set. In particular, the CSFs of $^{27}\text{Al}^+$ and $^{25}\text{Mg}^+$ are generated by single and restricted double (SrD) substitutions from core and valence orbitals, limiting the excitations to a maximum of one hole in the core. To describe the electron correlations, the first-order correlation is further separated into the correlation between the valence electrons (VV correlation), the correlation between valence and core electrons (CV correlation), and the correlation between core electrons (CC correlation). For $^{27}\text{Al}^+$ and $^{25}\text{Mg}^+$ ions, only the CV and VV correlations are taken into account, while for $^9\text{Be}^+$, all three

correlations are considered.

The orbital optimization in variational methods is achieved through an iterative process that requires initial estimates. Many difficulties can be avoided by adopting a systematic procedure where, instead of a large-scale calculation with many orthogonality constraints, a series of smaller calculations are performed with larger and larger orbital sets and the results from one are part of the input for the next. The maximum principal quantum number n of the active orbitals starts from two or three for the first layer and only increases by one per layer until it equals ten, and the angular quantum number l is set to the maximum by default. But in the test calculation, we found that some active orbitals with large l (such as $7i$, $8i$, $9i$ orbitals, *etc.*) had little contribution to the results and took up too many computing resources to slow down the overall computing speed. Therefore, these orbitals are not taken into account in this paper. In addition, the orbital sets of $^{27}\text{Al}^+$ formed in the layer $n = 10$ were fixed in subsequent relativistic configuration interaction (RCI) calculations in which the CSFs through single, double, and triple (SDT) substitutions from the reference configurations to orbitals within $5s$, $5p$, $4d$, and $4f$ were included.

Figure 2 shows the variation trends of the energy eigenvalues of the corresponding states in $^{27}\text{Al}^+$, $^9\text{Be}^+$, and $^{25}\text{Mg}^+$ ions along the calculation layers. As the number of configuration layers increases, the eigenvalue of each energy level gradually decreases and shows a convergence trend.

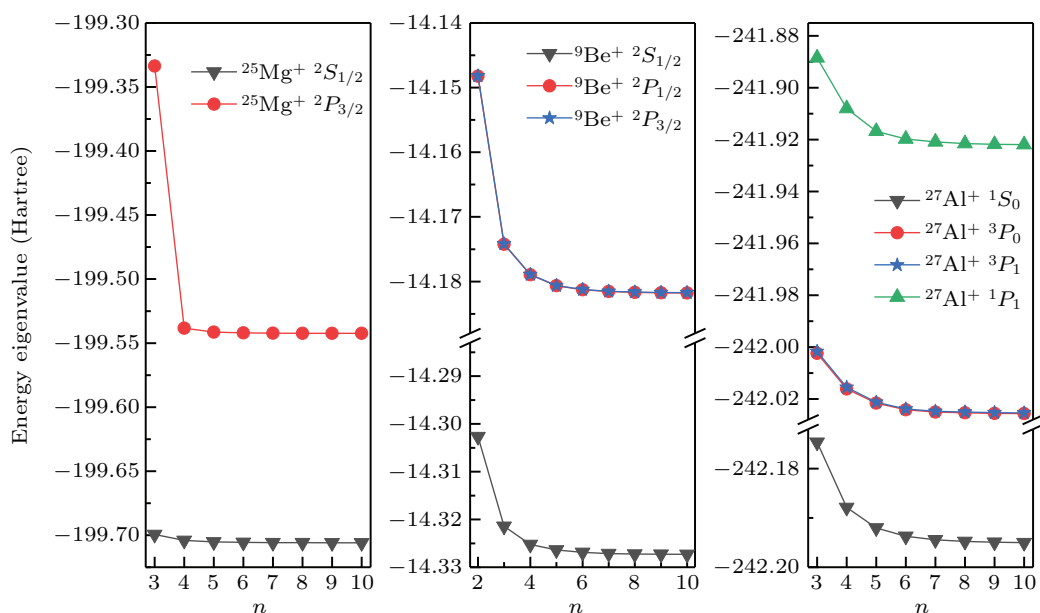


Fig. 2. Variations of the energy eigenvalues (in unit Hartree, 1 Hartree = 27.2114 eV) of the related energy levels in $^{27}\text{Al}^+$, $^9\text{Be}^+$, and $^{25}\text{Mg}^+$ ions along the calculation layer n . The abscissa n is the maximum quantum number of the active orbitals in the corresponding layer.

3. Results and discussions

Because the nuclear spins of $^{27}\text{Al}^+$, $^9\text{Be}^+$, and $^{25}\text{Mg}^+$ ions are not zero, their energy levels with non-zero angular momentum J have hyperfine structures whose precise measurements are essential parts in the optical clock experiment.

The hyperfine interaction constants of the related energy levels are given in Table 1. Our calculation model of Al^+ ion is similar to the one in Ref. [16], so the differences of the hyperfine interaction constants of the $3s3p\ ^1P_1$ state are within 0.6%. Since the high-order electron correlations and CC correlations

are not considered, there is a big difference in the hyperfine interaction constants of the $3s3p\ ^3P_1$ state. The uncertainty estimation method given in Refs. [47,48] is used to derive the uncertainty of the hyperfine interaction constants in Table 1.

By comparing the values in Table 1, we find that our magnetic dipole constants of $2s\ ^2S_{1/2}$ and $2p\ ^2P_{1/2}$ states of Be^+ are in good agreement with the experimental values, while the magnetic dipole constants of $3s\ ^2S_{1/2}$ state of Mg^+ is 3.6% higher than the experimental values. The reason why it is not as good as that in Ref. [24] may be that the main elec-

tron correlations in the calculation model of Mg^+ ion are less complete. The maximum differences between the hyperfine structure constants of $3p\ ^2P_{1/2}$ and $3p\ ^2P_{3/2}$ states of Mg^+ and others' theoretical values are 7.3% and 9.5%, respectively. For the magnetic dipole constant of the $2p\ ^2P_{3/2}$ state of Be^+ , the ratio of the uncertainty to the calculated value is 0.278. This is because there is no obvious linear relationship between the differences of the calculated values and the differences of the energy eigenvalues, so it is not suitable for the uncertainty estimation by the method given in Refs. [47,48].

Table 1. The hyperfine interaction constants of the related energy levels in $^{27}\text{Al}^+$, $^9\text{Be}^+$, and $^{25}\text{Mg}^+$ ions. A is the magnetic dipole constant (in unit MHz). B is the electric quadrupole constant (in unit MHz).

Constant	$\text{Be}^+ 2s\ ^2S_{1/2}$	$\text{Be}^+ 2p\ ^2P_{1/2}$	$\text{Be}^+ 2p\ ^2P_{3/2}$	$\text{Mg}^+ 3s\ ^2S_{1/2}$	$\text{Mg}^+ 3p\ ^2P_{1/2}$	$\text{Mg}^+ 3p\ ^2P_{3/2}$	$\text{Al}^+ 3s3p\ ^3P_1$	$\text{Al}^+ 3s3p\ ^1P_1$
				this work				
A (MHz)	-623.50(6.33)	-117.48(1.14)	-1.0594(2940)	-617.65(18.00)	-109.08(3.57)	-20.691(558)	1379.3(3.23)	196.24(3.26)
B (MHz)			-2.2607(636)			24.092(810)	-16.083(534)	22.235(259)
				others' theoretical data				
A (MHz)	-625.11(3) ^[18]	-117.925(4) ^[18]	-1.016(3) ^[18]	-592.86 ^[23]	-101.70 ^[23]	-18.89 ^[23]	1327.3(10.2) ^[16]	197.1(2.8) ^[16]
	-625.3927(36) ^[19]	-117.932(3) ^[20]	-1.026(3) ^[20]	-596.785 ^[24]	-102.997 ^[24]	-19.546 ^[24]	1389.814 ^[17]	286.0800 ^[17]
B (MHz)			-2.281(6) ^[18]			22.91 ^[23]	-15.1(0.2) ^[16]	22.1(0.3) ^[16]
			-2.29940(3) ^[20]				-16.646 ^[17]	28.308 ^[17]
				others' experimental data				
A (MHz)	-625.00883705(1) ^[42]	-118.6(36) ^[43]		-596.254376(54) ^[44]				
	-624.97(4) ^[45]	-118.00(4) ^[45]		-596.2542487(42) ^[46]				
				-596.254250949(45) ^[14]				

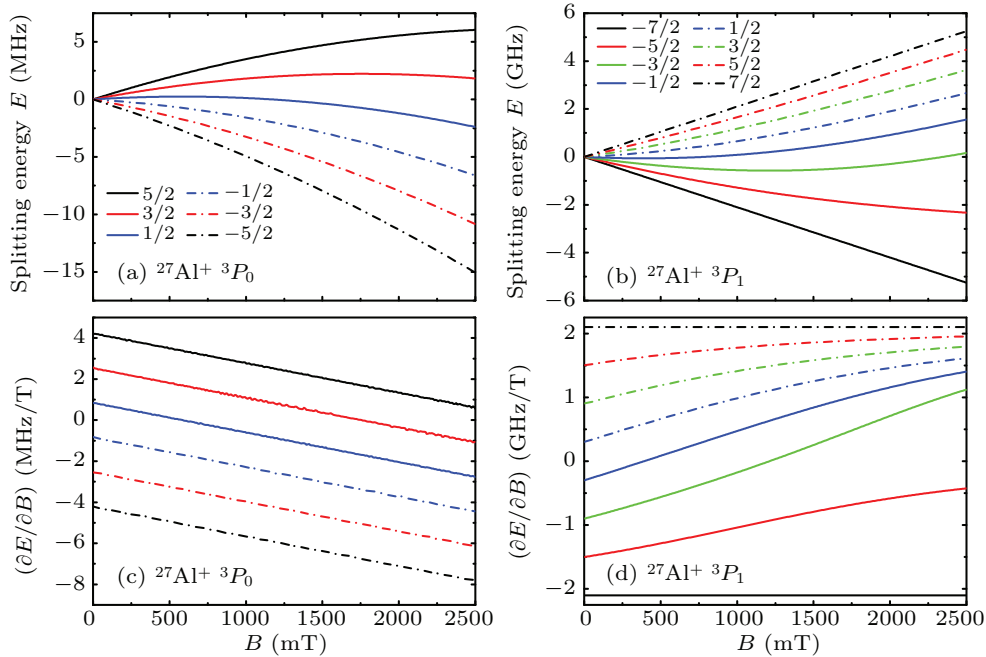


Fig. 3. The Zeeman shifts of the 3P_0 and 3P_1 states in $^{27}\text{Al}^+$ as functions of the magnetic field B . Splitting energy E is the Zeeman splitting value, and $\partial E/\partial B$ is the partial derivative of splitting energy E with respect to magnetic field B . Different curves correspond to Zeeman sublevels with different m_F values.

Figure 3 shows the magnetic sublevels of $3s3p\ ^3P_{0,1}$ state in $^{27}\text{Al}^+$. From the partial derivative curves in Fig. 3(c), it is clear that the Zeeman effect of 3P_0 is mainly first-order and second-order, so the Zeeman shifts can be approximately expressed as $E = C_1B + C_2B^2$, where C_1 and C_2 are coefficients that account for the linear and quadratic Zee-

man effects. According to the formula above, we can get that the first-order coefficients C_1 of the $|^3P_0, m_F = \pm 5/2\rangle$ are ± 4.22 MHz/T, respectively, and the second-order coefficients C_2 are -72.1831 MHz/T² and -72.1715 MHz/T², respectively. These second-order coefficients are not more than 0.34% different from the experimental values

$-71.944(24)$ MHz/T²^[14] and $-71.988(48)$ MHz/T².^[12] The factors that contribute to these tiny deviations include the facts that the splitting of the 1S_0 state in the magnetic field is very small, and the experimental Zeeman coefficients are obtained by measuring the $|^1S_0, m_F = \pm 5/2\rangle \rightarrow |^3P_0, m_{F'} = \pm 5/2\rangle$ transitions instead of the 3P_0 state. The difference in C_1 between two adjacent levels such as $m_F = 5/2$ and $m_F = 3/2$ is a constant, 1.69 MHz/T and the values of C_2 for all the states are quite close to each other. Compared with other states in this paper, the changes of Zeeman shifts of $3s3p\ ^3P_0$ states are particularly regular, which may be one of the important factors helping the aluminum ion clock to bust into new precision regime.^[9]

In Figs. 3(b) and 3(d), the curves ($m_F = \pm 7/2$) at the top and bottom edges of the graphs are roughly linear. The first-order coefficients of them are ± 2.1009 GHz/T, respectively, with only 0.04% deviations from the experimental value 2.100056 GHz/T in Ref. [49]. Because it is not feasible to directly measure the 3P_0 state, the experimental Zeeman coefficient is also obtained by measuring the first-order sensitive $|^1S_0, m_F = 5/2\rangle \rightarrow |^3P_1, m_{F'} = 7/2\rangle$ transition between qubit states. In addition, the sublevels that are closer to the center of Fig. 3(b) show more obvious high-order Zeeman effects.

The Zeeman splitting of the $^2S_{1/2}$ state in $^{25}\text{Mg}^+$ along the magnetic field is given in Fig. 4. The Zeeman shifts of the $|3, \pm 3\rangle$ sublevels in Figs. 4(a) and 4(b) are approximately linear when the magnetic field strength is in the range of 0–2000 mT, and the linear coefficients are -1.4012 GHz/T and 1.4012 GHz/T, respectively. We can find a significant transition from low field, where I and J are coupled to form the total angular momentum F , to high field, where they are decoupled. When the magnetic field strength is close to 2000 mT, the Zeeman shift of each sublevel begins to change linearly and approach the linear coefficients of the $|3, \pm 3\rangle$ sublevels.

For the $|3, 0\rangle \rightarrow |2, 0\rangle$ transition in Fig. 4, the quadratic Zeeman coefficients of these two sublevels are opposite in sign and equal in magnitude, that is, the sum of them is always near zero. Therefore, the high-order Zeeman effect of this transition is small compare to the ones of other transitions and can be used to measure the ground-state hyperfine interaction constant.^[46] This transition is also second-order sensitive to the external magnetic field and is used to determine $\langle B^2 \rangle$.^[14] For the $|3, -3\rangle \rightarrow |2, -2\rangle$ transition, the lower level $|3, -3\rangle$ has only the first-order Zeeman effect, and the upper level $|2, -2\rangle$ has the weakest second-order Zeeman effect in the splitting of the level $F = 2$, so this transition is first-order sensitive to the external magnetic field and is used to determine the DC component of $\langle B^2 \rangle$ in real-time.^[14]

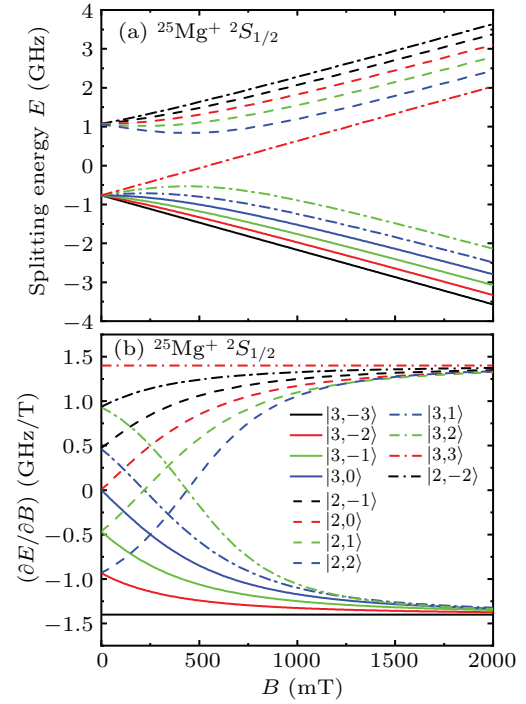


Fig. 4. The Zeeman shifts of the $^2S_{1/2}$ state in $^{25}\text{Mg}^+$ as functions of the magnetic field B . Splitting energy E is the Zeeman splitting value, and $\partial E/\partial B$ is the partial derivative of splitting energy E with respect to magnetic field B . Different curves correspond to Zeeman sublevels with different $|F, m_F\rangle$.

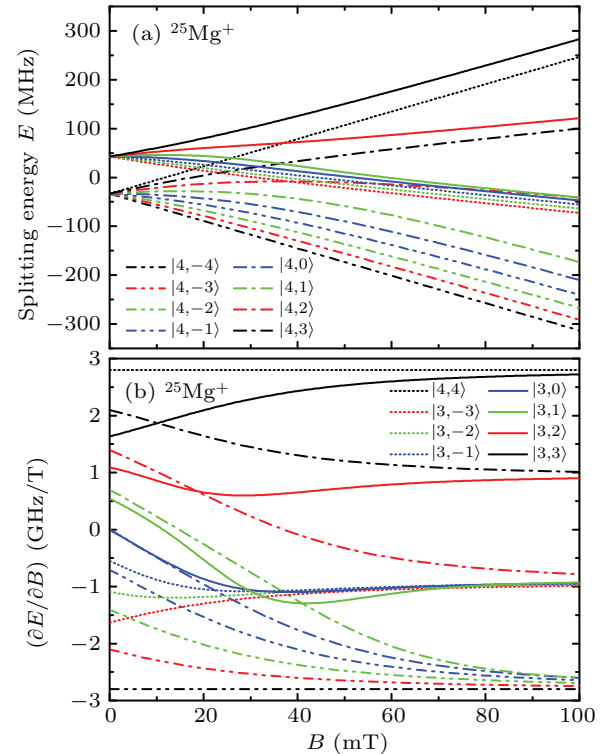


Fig. 5. The Zeeman shifts of the $^2P_{3/2}$ ($F = 4, 3$) state in $^{25}\text{Mg}^+$ as functions of the magnetic field B . Splitting energy E is the Zeeman splitting value, and $\partial E/\partial B$ is the partial derivative of splitting energy E with respect to magnetic field B . Different curves correspond to Zeeman sublevels with different $|F, m_F\rangle$.

Figure 5 shows the Zeeman splitting of the $^2P_{3/2}$ ($F = 4, 3$) state in $^{25}\text{Mg}^+$ in the magnetic field, and the decoupling of angular momentums in high magnetic field is more complicated than that in Fig. 4. When the magnetic field

strength increases to about 20 mT, the curves of sublevels split from $F = 4$ and $F = 3$ levels intersect. Once the magnetic field strength exceeds 90 mT, the Zeeman shifts of all sublevels tend to change linearly. The linear coefficients of the $|4, \pm 4\rangle$ levels at the top and bottom edges of Fig. 5(b) are ± 2.800755 GHz/T, respectively. When the magnetic field strength is within 10 mT, these energy sublevels mainly show the first-order and second-order Zeeman effects.

The Zeeman splitting of the $^2S_{1/2}$ state of $^9\text{Be}^+$ along the magnetic field in Fig. 6 is similar to that of $^{25}\text{Mg}^+$ in Fig. 4. When the magnetic field strength is more than 1500 mT, the Zeeman shifts of the sublevels in $^9\text{Be}^+$ show linear trends, and the change rates along the magnetic field begin to get closer to those of $|2, \pm 2\rangle$ levels. The linear coefficients of the $|2, \pm 2\rangle$ levels are ± 1.40122 GHz/T, respectively, with 0.02 MHz/T deviations from the linear coefficients of the $|2, \pm 2\rangle$ sublevels of the $^2S_{1/2}$ state in $^{25}\text{Mg}^+$.

Among the sublevels that intersect the vertical axis in Fig. 6(c), only the $|2, 0\rangle$ and $|1, 0\rangle$ sublevels are symmetric about $\partial E/\partial B = 0$, and the sum of the Zeeman coefficients of these two sublevels is always 309.49963 MHz instead of the case in $^{25}\text{Mg}^+$ where the sum is zero. Therefore, the second-order Zeeman effects of the $|2, 0\rangle \rightarrow |1, 0\rangle$ transition cancel out, and this transition is generally used to study the first-order Zeeman effects. The $|2, -2\rangle$ sublevel only has first-order effect, the Zeeman effects above second order of the $|1, -1\rangle$ sublevel are weak, and both are at the outermost side of the sublevels split from the same level. In consequence, these two transitions are generally measured experimentally to study the effect of the magnetic field on the energy level structure of the

$^2S_{1/2}$ state in $^9\text{Be}^+$. Besides, the $|2, -2\rangle$ and $|2, 2\rangle$ sublevels of the $^2P_{1/2}$ state in $^9\text{Be}^+$ have second-order Zeeman effects that are small compared to other sublevels, so it is not easy to observe directly from Figs. 6(b) and 6(d). Based on the calculation data, we obtain that the first-order coefficients of $|2, 2\rangle$ and $|2, -2\rangle$ sublevels in $^9\text{Be}^+$ are ± 0.46574 GHz/T, respectively, and the second-order coefficients are -1.53333 MHz/T² and -1.53286 MHz/T², respectively.

Figure 7 shows the Zeeman shifts of the $^2P_{3/2}$ states in $^9\text{Be}^+$ as functions of the magnetic field. When in the high magnetic field, due to the decoupling of the angular momentums, the sixteen curves of the sublevels of the $^2P_{3/2}$ states in Fig. 7(a) can be evenly divided into four groups according to m_J , with four curves in each group tending to be linear and roughly parallel. Specifically, the first-order coefficients of the $|3, -3\rangle$, $|3, -2\rangle$, $|3, -1\rangle$, and $|3, 0\rangle$ sublevels in the first group are all -2.80078 GHz/T, the first-order coefficients of the $|2, -2\rangle$, $|2, -1\rangle$, $|2, 0\rangle$, and $|3, 1\rangle$ sublevels in the second group are all -0.931 GHz/T, the first-order coefficients of the $|1, -1\rangle$, $|1, 0\rangle$, $|2, 1\rangle$, and $|3, 2\rangle$ sublevels in the third group are all 0.936 GHz/T, and the first-order coefficients of the $|0, 0\rangle$, $|1, 1\rangle$, $|2, 2\rangle$, and $|3, 3\rangle$ sublevels in the fourth group are all 2.80078 GHz/T. These linear coefficients are only applicable in the magnetic field above 400 mT, and the linear coefficients of the outer sublevels have more precise digits. Especially for the first and fourth groups, the coefficients are equal in magnitude. Among these sublevels, the outermost $|3, \pm 3\rangle$ sublevels often considered in experiments mainly have the first-order Zeeman effects.

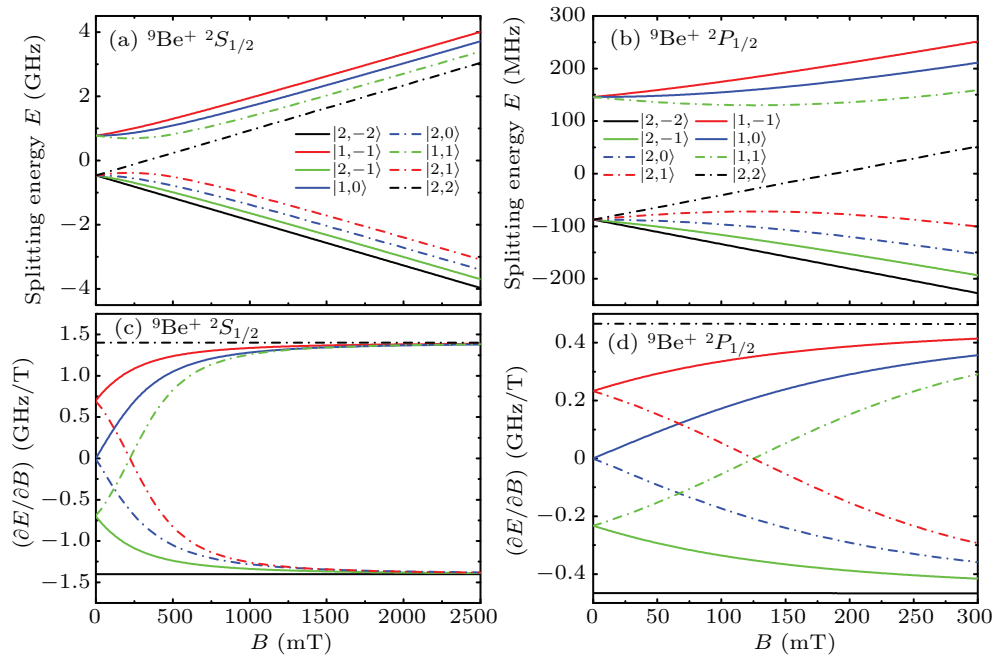


Fig. 6. The Zeeman shifts of the $^2S_{1/2}$ and $^2P_{1/2}$ states in $^9\text{Be}^+$ as functions of the magnetic field B . Splitting energy E is the Zeeman splitting value, and $\partial E/\partial B$ is the partial derivative of splitting energy E with respect to magnetic field B . Different curves correspond to Zeeman sublevels with different $|F, m_F\rangle$.

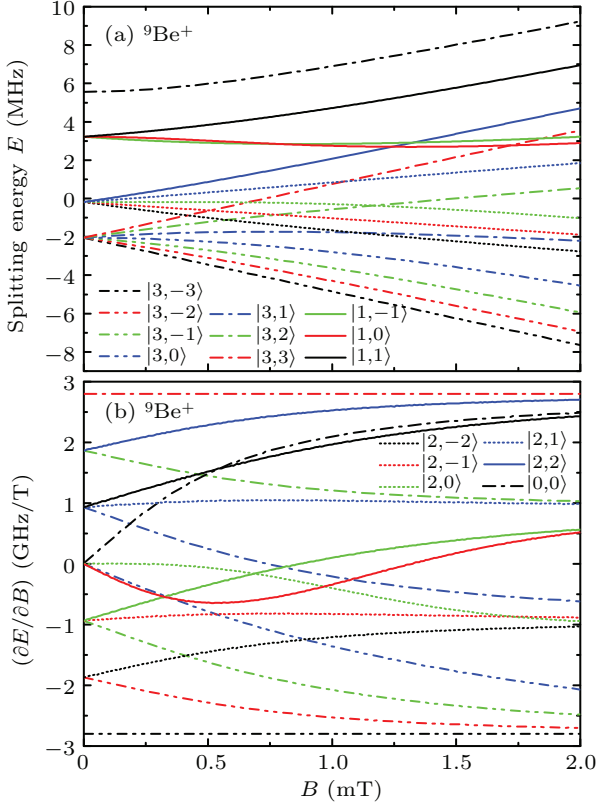


Fig. 7. The Zeeman shifts of the $^2P_{3/2}$ states in $^9\text{Be}^+$ as functions of the magnetic field B . Splitting energy E is the Zeeman splitting value, and $\partial E/\partial B$ is the partial derivative of splitting energy E with respect to magnetic field B . Different curves correspond to Zeeman sublevels with different $|F, m_F\rangle$.

From the Zeeman splittings in Figs. 3–7, we can see that the Zeeman energies of the $m_F = \pm F$ states in which the F is the maximum F value for a reference configuration change linearly with increasing B for all field strengths because their wavefunctions are not mixed. For other states, the magnetic

effect tends to be first-order as B increases in the high-field regime. This is because the I and J are decoupled and the Zeeman interaction dominates when the magnetic field is very strong, the eigenstates are well described by the $|I, m_I; J, m_J\rangle$ basis.

In addition to the hyperfine interaction constants and Zeeman shifts of the related levels in $^{27}\text{Al}^+$, $^9\text{Be}^+$, and $^{25}\text{Mg}^+$ ions, we also calculate the isotope shift parameters of these levels, and the results are shown in Table 2. Compared with the theoretical values in Ref. [16], the deviations of ΔK_{NMS} , ΔK_{SMS} , and ΔF of the $^1S_0 \rightarrow ^3P_1$ transition in $^{27}\text{Al}^+$ are 2%, 1.8%, and 2.5%, respectively. However, the SMS parameter of the $^1S_0 \rightarrow ^1P_1$ transition in $^{27}\text{Al}^+$ is quite different from that in Ref. [16], it is mainly because the SMS parameter is sensitive to the electron correlation, and the captures of the CC correlations and high-order correlations make the results different.

Table 2. The normal mass shift parameters K_{NMS} (in unit GHz-u), the specific mass shift parameters K_{SMS} (in unit GHz-u), and the field shift parameters F (in unit a.u.) of the related energy levels in Al^+ , Be^+ , and Mg^+ ions.

Term	K_{NMS} (GHz-u)	K_{SMS} (GHz-u)	F (a.u.)
$\text{Al}^+ \ ^1S_0$	872110.21(131.64)	-126396.27(50.60)	1498.3215(2375)
$\text{Al}^+ \ ^3P_0$	871456.18(21.78)	-127368.06(80.42)	1495.1037(1669)
$\text{Al}^+ \ ^3P_1$	871457.45(13.17)	-127366.34(70.38)	1495.0968(1661)
$\text{Al}^+ \ ^1P_1$	871117.78(74.23)	-126343.41(119.39)	1495.2792(2002)
$\text{Mg}^+ \ ^2S_{1/2}$	719246.265(5.355)	-98776.62(43.19)	1156.0517(252)
$\text{Mg}^+ \ ^2P_{1/2}$	718777.927(8.402)	-99229.33(16.32)	1153.9916(11)
$\text{Mg}^+ \ ^2P_{3/2}$	718777.589(5.147)	-99229.83(15.05)	1153.9913(3)
$\text{Be}^+ \ ^2S_{1/2}$	51698.374(1.096)	1633.14(12.54)	35.3569(7)
$\text{Be}^+ \ ^2P_{1/2}$	51172.150(2.677)	600.86(66.25)	34.4924(6)
$\text{Be}^+ \ ^2P_{3/2}$	51172.278(2.623)	600.64(66.27)	34.4925(7)

Table 3. Comparison of our theoretical predictions with the experimental results of isotope shifts of D1 and D2 lines for different Mg^+ or Be^+ isotope pairs. The D1 line and the D2 line of Mg^+ correspond to the $3s \ ^2S_{1/2} \rightarrow 3p \ ^2P_{1/2}$ transition and $3s \ ^2S_{1/2} \rightarrow 3p \ ^2P_{3/2}$ transition, respectively. The D1 line and the D2 line of Be^+ correspond to the $2s \ ^2S_{1/2} \rightarrow 2p \ ^2P_{1/2}$ transition and the $2s \ ^2S_{1/2} \rightarrow 2p \ ^2P_{3/2}$ transition, respectively. All values are given in unit MHz.

Isotopes	D1	D2	Reference
$^{26}\text{Mg}^+ \text{--} ^{24}\text{Mg}^+$	3084.905(93)	3087.560(87)	Batteiger <i>et al.</i> ^[50]
		3050 ± 100	Drullinger <i>et al.</i> ^[51]
$^{25}\text{Mg}^+ \text{--} ^{24}\text{Mg}^+$	3045.9211(53.9337)	3047.1340(65.3869)	this work
	1620(19) ^a	1621(19) ^a	Batteiger <i>et al.</i> ^[50]
$^{26}\text{Mg}^+ \text{--} ^{25}\text{Mg}^+$	1599.9583(92.0315)	1600.5907(34.3405)	this work
	1461 ± 100		Drullinger <i>et al.</i> ^[51]
$^7\text{Be}^+ \text{--} ^9\text{Be}^+$	1445.9628(26.5630)	1446.5433(31.0464)	this work
	-49236.9(9)	-49242.1(2.0)	Nörtershäuser <i>et al.</i> ^[45]
	-49236.94(80)		Žáková <i>et al.</i> ^[52]
$^{10}\text{Be}^+ \text{--} ^9\text{Be}^+$	-49211.77(2380.66)	-49214.57(2380.56)	this work
	17323.8(13)		Nörtershäuser <i>et al.</i> ^[45]
	17323.82(82)	17327.3(2.0)	Žáková <i>et al.</i> ^[52]
$^{11}\text{Be}^+ \text{--} ^9\text{Be}^+$	17314.87(837.17)	17315.85(837.13)	this work
	31565.0(9)		Nörtershäuser <i>et al.</i> ^[45]
	31565.04(86)	31569.6(2.3)	Žáková <i>et al.</i> ^[52]
	31547.96(1526.27)	31549.75(1526.21)	this work

^aThe values are derived from the experimental values.

Currently, there is no experimental data on the isotope shifts of these transitions in $^{27}\text{Al}^+$ for assessing the advantages of the calculation models. The experimental and theoretical isotope shifts of the D1 and D2 lines in Be^+ and Mg^+ ions are given in Table 3, and a good agreement between the experimental results and our calculation results is obtained. The calculation errors for the isotope shifts of Mg^+ and Be^+ ions are less than 1.3% and 0.07%, respectively, indicating that our calculation model is reliable. Table 3 shows that the uncertainties of isotope shifts of Be^+ are relatively large and the ratios of the uncertainties to calculated values are about 0.048. However, the differences between the calculated results of Be^+ and the experimental values are below 0.07%, which is closer to the experimental values than that of Mg^+ . This is because δK or δF and the difference of energy eigenvalues do not show a close to linear correlation, *i.e.*, the linear uncertainty estimation method^[47,48] is not suitable for the current calculation model of Be^+ ion.

4. Conclusion

In this paper, we use the MCDHF method to calculate the hyperfine interaction constants, Zeeman shifts, and isotope shifts of the states in $^{27}\text{Al}^+$ ion and logic ions $^9\text{Be}^+$ and $^{25}\text{Mg}^+$ that are involved in the $^{27}\text{Al}^+$ optical clock. We analyze the influence of the external magnetic field on these hyperfine structure energy levels, and the Zeeman shifts are given. These results will be helpful for better evaluation of systematic uncertainty of the $^{27}\text{Al}^+$ optical clock. The calculation of isotope shift parameters can provide important reference data for the spectroscopic measurement of nuclear charge radius which is a necessary theoretical basis to study the structures, properties and nucleon interaction law of these three elements.

References

- [1] Rosenband T, Hume D B, Schmidt P O, Chou C W, Brusch A, Lorini L, Oskay W H, Drullinger R E, Fortier T M, Stalnaker J E, Diddams S A, Swann W C, Newbury N R, Itano W M, Wineland D J and Bergquist J C 2008 *Science* **319** 1808
- [2] Godun R M, Nisbet-Jones P B R, Jones J M, King S A, Johnson L A M, Margolis H S, Szymaniec K, Lea S N, Bongs K and Gill P 2014 *Phys. Rev. Lett.* **113** 210801
- [3] Chou C, Hume D, Koelemeij J, Wineland D and Rosenband T 2010 *Phys. Rev. Lett.* **104** 070802
- [4] Chou C W, Hume D B, Rosenband T and Wineland D J 2010 *Science* **329** 1630
- [5] Grotti J, Koller S, Vogt S, Häfner S, Sterr U, Lisdat C, Denker H, Voigt C, Timmen L, Rolland A, Baynes F N, Margolis H S, Zampaolo M, Thoumany P, Pizzocaro M, Rauf B, Bregolin F, Tampellini A, Barbieri P, Zucco M, Costanzo G A, Clivati C, Levi F and Calonico D 2018 *Nat. Phys.* **14** 437
- [6] Graham P W, Hogan J M, Kasevich M A and Rajendran S 2013 *Phys. Rev. Lett.* **110** 171102
- [7] Roberts B M, Blewitt G, Dailey C, Murphy M, Pospelov M, Rollings A, Sherman J, Williams W and Derevianko A 2017 *Nat. Commun.* **8** 1195
- [8] Kennedy C J, Oelker E, Robinson J M, Bothwell T, Kedar D, Milner W R, Marti G E, Derevianko A and Ye J 2020 *Phys. Rev. Lett.* **125** 201302
- [9] Brewer S M, Chen J-S, Hankin A M, Clements E R, Chou C W, Wineland D J, Hume D B and Leibbrandt D R 2019 *Phys. Rev. Lett.* **123** 033201
- [10] Ludlow A D, Boyd M M, Ye J, Peik E and Schmidt P O 2015 *Rev. Mod. Phys.* **87** 637
- [11] Schmidt P O 2005 *Science* **309** 749
- [12] Rosenband T, Schmidt P, Hume D, Itano W, Fortier T, Stalnaker J, Kim K, Diddams S, Koelemeij J, Bergquist J and Wineland D 2007 *Phys. Rev. Lett.* **98** 220801
- [13] Bernard J E, Marmet L and Madej A A 1998 *Opt. Commun.* **150** 170
- [14] Brewer S M, Chen J-S, Beloy K, Hankin A M, Clements E R, Chou C W, McGrew W F, Zhang X, Fasano R J, Nicolodi D, Leopardi H, Fortier T M, Diddams S A, Ludlow A D, Wineland D J, Leibbrandt D R and Hume D B 2019 *Phys. Rev. A* **100** 013409
- [15] Gan H C J, Maslennikov G, Tseng K W, Tan T R, Kaewuam R, Arnold K J, Matsukevich D and Barrett M D 2018 *Phys. Rev. A* **98** 032514
- [16] Zhang T, Xie L, Li J and Lu Z 2017 *Phys. Rev. A* **96** 012514
- [17] Kumar R, Chattopadhyay S, Angom D and Mani B K 2021 *Phys. Rev. A* **103** 022801
- [18] Yerokhin V A 2008 *Phys. Rev. A* **78** 012513
- [19] Puchalski M and Pachucki K 2014 *Phys. Rev. A* **89** 032510
- [20] Puchalski M and Pachucki K 2009 *Phys. Rev. A* **79** 032510
- [21] Yan Z C, Nörtershäuser W and Drake G W F 2008 *Phys. Rev. Lett.* **100** 243002
- [22] Puchalski M and Pachucki K 2008 *Phys. Rev. A* **78** 052511
- [23] Sur C, Sahoo B K, Chaudhuri R K, Das B P and Mukherjee D 2005 *Eur. Phys. J. D* **32** 25
- [24] Mani B K and Angom D 2010 *Phys. Rev. A* **81** 042514
- [25] Tupitsyn I I, Shabaev V M, Crespo López-Urrutia J R, Draganić I, Soria Orts R and Ullrich J 2003 *Phys. Rev. A* **68** 022511
- [26] Safronova M S and Johnson W R 2001 *Phys. Rev. A* **64** 052501
- [27] Berengut J C, Dzuba V A and Flambaum V V 2003 *Phys. Rev. A* **68** 022502
- [28] Korol V A and Kozlov M 2007 *Phys. Rev. A* **76** 022103
- [29] Yu G H, Yan H, Gao D L, Zhao P Y, Liu H, Zhu X L and Yang W 2018 *Acta Phys. Sin.* **67** 013101 (in Chinese)
- [30] Grant I P 2007 *Relativistic quantum theory of atoms and molecules: theory and computation* (New York: Springer) pp. 259–388
- [31] Jönsson P, Gaigalas G, Bieroń J, Fischer C F and Grant I P 2013 *Comput. Phys. Commun.* **184** 2197
- [32] Andersson M and Jönsson P 2008 *Comput. Phys. Commun.* **178** 156
- [33] Stone N J 2005 *At. Data Nucl. Data Tables* **90** 75
- [34] Jönsson P, Parpia F A and Fischer C F 1996 *Comput. Phys. Commun.* **96** 301
- [35] Cheng K T and Childs W J 1985 *Phys. Rev. A* **31** 2775
- [36] Li W, Grumer J, Brage T and Jönsson P 2020 *Comput. Phys. Commun.* **253** 107211
- [37] Palmer C W P 1987 *J. Phys. B: At. Mol. Phys.* **20** 5987
- [38] Blundell S A, Baird P E G, Palmer C W P, Stacey D N and Woodgate G K 1987 *J. Phys. B: At. Mol. Phys.* **20** 3663
- [39] Angeli I and Marinova K P 2013 *At. Data Nucl. Data Tables* **99** 69
- [40] Ekman J, Jönsson P, Godefroid M, Nazé C, Gaigalas G and Bieroń J 2019 *Comput. Phys. Commun.* **235** 433
- [41] Froese Fischer C, Brage T and Jönsson P 1997 *Computational atomic structure: an MCHF approach* (London: Institute of Physics Publishing) pp. 67–86
- [42] Wineland D J, Bollinger J J and Itano W M 1983 *Phys. Rev. Lett.* **50** 628
- [43] Bollinger J J, Wells J S, Wineland D J and Itano W M 1985 *Phys. Rev. A* **31** 2711
- [44] Itano W M and Wineland D J 1981 *Phys. Rev. A* **24** 1364
- [45] Nörtershäuser W, Tiedemann D, Žáková M, Andjelkovic Z, Blaum K, Bissell M L, Cazan R, Drake G W F, Geppert Ch, Kowalska M, Krämer J, Krieger A, Neugart R, Sánchez R, Schmidt-Kaler F, Yan Z C, Yordanov D T and Zimmermann C 2009 *Phys. Rev. Lett.* **102** 062503
- [46] Xu Z T, Deng K, Che H, Yuan W H, Zhang J and Lu Z H 2017 *Phys. Rev. A* **96** 052507
- [47] Carette T and Godefroid M R 2011 *Phys. Rev. A* **83** 062505
- [48] Zhang T X, Li J G and Liu J P 2018 *Acta Phys. Sin.* **67** 053101 (in Chinese)
- [49] Guggemos M, Guevara-Bertsch M, Heinrich D, Herrera-Sancho O A, Colombe Y, Blatt R and Roos C F 2019 *New J. Phys.* **21** 103003
- [50] Batteiger V, Knünz S, Herrmann M, Saathoff G, Schüssler H A, Bernhardt B, Wilken T, Holzwarth R, Hänsch T W and Udem Th 2009 *Phys. Rev. A* **80** 022503
- [51] Drullinger R E, Wineland D J and Bergquist J C 1980 *Appl. Phys.* **22** 365
- [52] Žáková M, Andjelkovic Z, Bissell M L, Blaum K, Drake G W F, Geppert C, Kowalska M, Krämer J, Krieger A, Lochmann M, Neff T, Neugart R, Nörtershäuser W, Sánchez R, Schmidt-Kaler F, Tiedemann D, Yan Z C, Yordanov D T and Zimmermann C 2010 *J. Phys. G: Nucl. Part. Phys.* **37** 055107